

Research Article

Synthesis of Nickel-Zinc Ferrite Nanoparticles by the Sol-Gel Auto-Combustion Method: Study of Crystal Structural, Cation Distribution, and Magnetic Properties

Sarwar Hasan ¹ and Bruska Azhdar ²

¹Azmar College for Gifted Students, Sulaimani Directorate of Education, Sulaimani, Iraq

²Nanotechnology Research Laboratory, Department of Physics, College of Science, University of Sulaimani, Sulaimani, Iraq

Correspondence should be addressed to Bruska Azhdar; bruska.azhdar@univsul.edu.iq

Received 13 February 2022; Accepted 8 May 2022; Published 28 May 2022

Academic Editor: Gary Wysin

Copyright © 2022 Sarwar Hasan and Bruska Azhdar. This is an open access article distributed under the Creative Commons Attribution License, which permits unrestricted use, distribution, and reproduction in any medium, provided the original work is properly cited.

Spinel ferrite nanocomposites of $\text{Ni}_{1-x}\text{Zn}_x\text{Fe}_2\text{O}_4$ ($x = 0.25$ and 0.75) were synthesized by sol-gel auto-combustion and annealed between 250°C and 1000°C . A single-phase spinel structure was found through X-ray diffraction (XRD). The crystallite size is in the range of $17.55\text{--}66.98$ nm, and lattice parameters are in the range of $8.351\text{--}8.434$ Å. X-ray analysis revealed a slight shift of the peaks towards shorter angles when the zinc concentration increased from 0.25 to 0.75 . XRD measurements revealed the metal ion distribution in the spinel ferrite system. For each sample, XRD data were used to compute structural characteristics such as lattice spacing, lattice constant, crystallite size, oxygen position parameter, tetrahedral and octahedral ionic radii, and bond lengths. Energy dispersive spectroscopy (EDS) spectra and field emission-electron scanning microscope (FESEM) were used to evaluate the elemental content and morphology. EDS analysis confirmed the presence of expected elements in the samples and confirmed the high doping rate of more than 180% of Zn ions in Ni ferrite. The evaluated particle sizes were determined to be 79.2 and 118.4 nm for zinc content of 0.25 and 0.75 , respectively. The nearly spherical shape of the nanoparticles was shown in the transmission electron microscope (TEM). The magnetic moment, remanent, coercivity, and saturation magnetization were calculated by using vibrating sample magnetometer (VSM) results. The saturation magnetization magnitudes showed the influence of cation distribution.

1. Introduction

Spinel ferrite has been developed by a huge number of researchers and scientists in recent decades due to its versatile and unusual structural, spectroscopic, and magnetic properties [1]. Spinel ferrites have applications in microwaves [2], drug delivery [3], gas sensors [4, 5], and electronic devices [6], all of which are associated with the type of transition metals in their network [7]. Low porosity, high density, and specified microstructure are required for their technological applications [8].

The investigated ferrite nanopowder forms spinel crystals. It follows the $F\bar{d}3m$ space group. According to their lattice environments, the divalent A and trivalent B cations occupy the octahedral or tetrahedral sites,

respectively. The spinel ferrites are classified into two types based on the distribution of A^{2+} and Fe^{3+} cations on (A) or [B] sites: normal spinel AB_2O_4 with the formula $(\text{A}^{2+})_A[\text{Fe}^{3+}\text{Fe}^{3+}]_B\text{O}_4^{2-}$, and the inverse type B (AB) O_4 with the formula $(\text{A}^{2+}\text{Fe}^{3+})_A[\text{A}^{2+}\text{Fe}^{3+}]_B\text{O}_4^{2-}$ [9]. Figure 1 demonstrates that spinel ferrites crystallize [10], and the metal ion is trapped in the void between the oxygen ions because its radius is lower than the oxygen ion radius. The occupancy of cations along the (A) and [B] sites affects the structural and magnetic properties of spinel ferrites [11, 12].

In bulk nickel-zinc (Ni-Zn) ferrite systems, the zinc ions prefer the tetrahedral position, and the nickel ions prefer the octahedral position. However, it has been shown that a small percentage of zinc and nickel ions might also be found in the

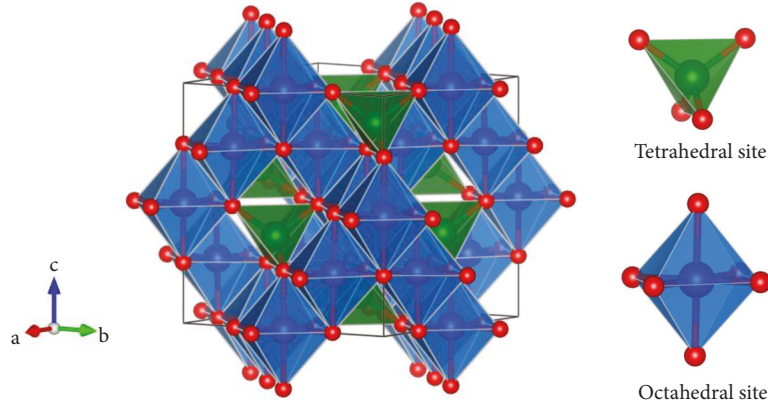


FIGURE 1: The cubic spinel structure. The oxygen locations are shown in red, while the tetrahedral and octahedral cation sites are indicated in green and blue, respectively.

nanocrystalline form, occupying the octahedral and tetrahedral positions, respectively [13].

Ni-Zn spinel ferrites are remarkably exciting for their high magnetic permeability, low electrical conductivity, and good performance at high frequencies [14]. Many methods were used to manufacture the Ni-Zn nanoferrite, including the hydrothermal approach [15], coprecipitation [16], sol-gel [17], microwave combustion [18], and others [19, 20]. One of the most convenient and effective approaches among these is the sol-gel approach. The sol-gel process has been successfully used to achieve small and uniform particle size, chemical homogeneity, high purity, and energy savings [21]. Regarding the microscopic properties, parameters such as composition, grain size, dopant amount, impurities, production process, and heating conditions are significant for Ni-Zn ferrites [22].

The purpose of this research was to study the influence of the composition of nanosized $\text{Ni}_{1-x}\text{Zn}_x\text{Fe}_2\text{O}_4$ ferrites with $x=0.25$ and 0.75 on crystal structure, cation distribution, and magnetic characteristics.

2. Experimental Procedures

The sol-gel auto-combustion technique was used to synthesize $\text{Ni}_{1-x}\text{Zn}_x\text{Fe}_2\text{O}_4$ powders ($x=0.25$ and 0.75). The analytical grade metal nitrates $\text{Ni}(\text{NO}_3)_2 \cdot 6\text{H}_2\text{O}$, $\text{Fe}(\text{NO}_3)_3 \cdot 9\text{H}_2\text{O}$, and $\text{Zn}(\text{NO}_3)_2 \cdot 6\text{H}_2\text{O}$ from BIOCHEM Chemopharma are used as the starting precursor materials. The stoichiometric amount of raw materials with citric acid (metal nitrate to citrate ratio was 1 : 2.2) was dissolved with minimum Milli-Q water and mixed under ultrasonic for 10 minutes. The temperature was then raised to 90°C , resulting in the formation of the brown viscous gel. It was placed in an oven at 200°C and auto-combustion occurred to form a fluffy powder. The fluffy powder was ultrasonicated in ethanol for 30 minutes to improve the obtained powder properties [23]. The produced powders were dried overnight at 80°C . Finally, the samples were annealed at temperatures of 250 , 500 , 750 , and 1000°C by $10^\circ\text{C}/\text{min}$ for 4 hours.

The crystalline structure of the samples was examined by Panalytical's X'Pert Pro X-ray diffractometer (XRD). The

morphology and microstructural evolution of the produced powder particles were carried out through the transmission electron microscope (TEM), ZEISS MODEL EM10C-100 KV, and the field emission scanning electron microscope (FESEM), ZEISS MODEL SIGMA VP. Energy dispersive spectroscopy (EDS) was used to investigate the elemental composition. The Fourier transform infrared spectroscopy (FTIR) spectra were obtained in the range of $400\text{--}900\text{ cm}^{-1}$ using a Perkin Elmer Model, USA. The measurements of magnetic properties were carried out via a vibrating sample magnetometer (VSM, LBKFB model-Meghnatis Daghigh Kavir Company).

3. Results and Discussion

3.1. X-ray Diffractometer (XRD). Powder XRD patterns of the $\text{Ni}_{1-x}\text{Zn}_x\text{Fe}_2\text{O}_4$ samples annealed at 250 , 500 , 750 , and 1000°C are shown in Figure 2(a) for $x=0.25$ and Figure 2(b) for $x=0.75$. The peaks that appear in the graph indicated that the single-phase cubic spinel ferrites were formed at 750°C and 1000°C . At annealing temperatures of 500°C and below, the secondary phase of the Fe_2O_3 impurity was verified [24].

The maximum intensity of the peak was found in the (311) plane which indicated that in the direction of the (311) plane of diffraction, the nanoparticle grains were dominating. The oxidation during annealing and thermal decomposition was considered to have resulted in the formation of Fe_2O_3 [25]. By using Scherrer's equation as mentioned below, the crystallite size (D) of the samples was calculated [26] as

$$D_{\text{Sch}} = \frac{K\lambda}{\beta \cos \theta'} \quad (1)$$

where K is the shape function that equals 0.9 , λ is the X-ray wavelength of 0.1545 nm , and β is the full width at half maximum of the (311) peak and is the diffraction angle.

The lattice parameter (average of all peaks) (a_{avg}), bulk density (ρ_b), X-ray density (ρ_x), and porosity ($\%P$) of the samples were evaluated based on the following relations [27], and the results are listed in Table 1.

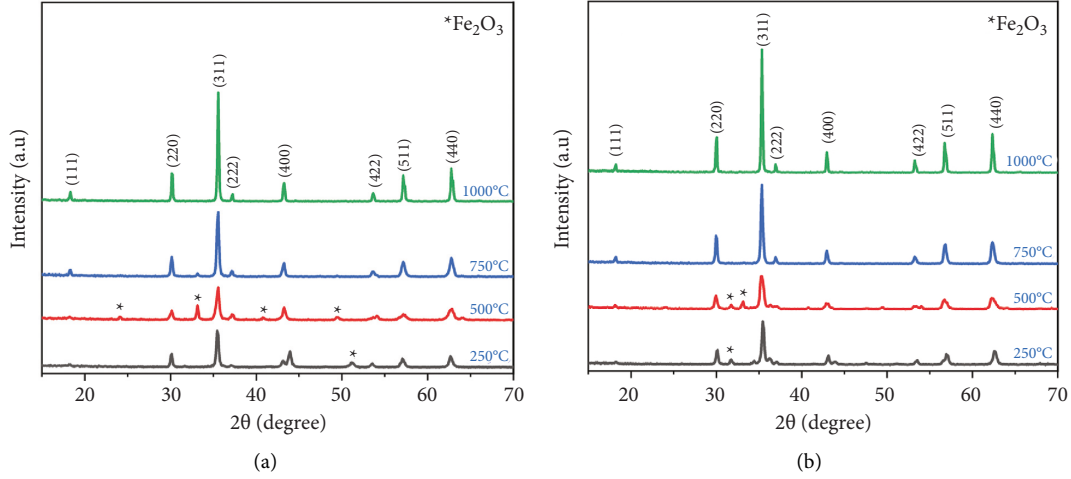


FIGURE 2: X-ray diffraction patterns of synthesized: (a) $\text{Ni}_{0.75}\text{Zn}_{0.25}\text{Fe}_2\text{O}_4$ and (b) $\text{Ni}_{0.25}\text{Zn}_{0.75}\text{Fe}_2\text{O}_4$ at different annealing temperatures.

TABLE 1: 2θ for maximum intensity, 2θ , d -spacing, d , average lattice parameter, a_{avg} , lattice parameter from NR plot, a_{NR} , unit cell volume, V , crystal sizes from Scherrer's method, D_{Sch} , crystal size from WH plot, D_{WH} , X-ray density, ρ_x (g/cm^3), and porosity, % P , of the samples at different annealing temperatures.

Structural parameters	250°C		500°C		750°C		1000°C	
	0.25	0.75	0.25	0.75	0.25	0.75	0.25	0.75
2θ (°)	35.45	35.45	35.55	35.25	35.55	35.35	35.55	35.35
d -spacing (Å)	2.530	2.530	2.523	2.544	2.523	2.537	2.523	2.537
a_{avg} (Å)	8.382	8.391	8.373	8.427	8.369	8.416	8.366	8.413
a_{NR} (Å)	8.364	8.385	8.351	8.413	8.362	8.424	8.372	8.434
V (Å ³)	588.90	590.80	587.01	598.44	586.17	596.10	585.54	595.46
ρ_x (g/cm^3)	5.325	5.384	5.342	5.315	5.350	5.335	5.355	5.340
% P	70.59	79.48	68.91	79.68	65.51	75.05	64.26	77.47
D_{Sch} (nm)	26.70	25.90	19.58	17.55	27.99	30.87	43.95	45.58
D_{WH} (nm)	26.26	18.51	18.79	22.40	45.31	47.16	66.98	62.18

$$a = d_{hkl} \sqrt{h^2 + k^2 + l^2}, \quad (2)$$

where d_{hkl} is the interplanar spacing, and (h, k, l) are the Miller indices.

$$\rho_b = \frac{\text{mass of the sample}}{\text{volume of the pallet}},$$

$$\rho_x = \frac{8M_w}{N_A a^3}, \quad (3)$$

$$\% P = \left(1 - \frac{\rho_b}{\rho_x}\right) \times 100,$$

where M_w is the molecular weight, N_A is Avogadro's number, and 8 is the number of formula units in a cell.

The Nelson–Riley (NR) plot provided the precise value of the lattice parameter (a). This approach was utilized to reduce mistakes induced by aberration of 2θ variation. Figure 3 shows a plot of lattice parameter (a) against $F(\theta)$ that was plotted and linearly fit. It is possible to obtain the corrected value of the lattice parameter stated in Table 1 by taking the intercept on the (a) axis [28].

$$F(\theta) = \frac{1}{2} \left[\frac{\cos^2 \theta}{\sin \theta} + \frac{\cos^2 \theta}{\theta} \right]. \quad (4)$$

The size of crystallites has also been approximated by using Williamson and Hall (WH) plots to separate size and strain broadening [29]. This approach relies on the widening of diffraction lines caused by crystallite size and internal strain.

$$\beta \cos \theta = \frac{\lambda}{D_{\text{WH}}} + \varepsilon(4 \sin \theta), \quad (5)$$

where β is measured for different XRD lines corresponding to different planes, θ is the Bragg angle, ε is the strain, and D_{WH} is the crystallite size. (5) represents a straight line between $4 \sin \theta$ (x -axis) and $\beta \cos \theta$ (y -axis). The value of D_{WH} is obtained by the intercept (λ/D_{WH}) of the line [30], and the values are listed in Table 1. Figures 4(a) and 4(b) show the linear fitting WH plots of $\text{Ni}_{0.75}\text{Zn}_{0.25}\text{Fe}_2\text{O}_4$ and $\text{Ni}_{0.25}\text{Zn}_{0.75}\text{Fe}_2\text{O}_4$, respectively.

The size of the crystallites increased as the temperature increased ($\geq 500^\circ\text{C}$). At a temperature of 1000°C , the crystallite size reached 43.46 nm and 45.08 nm for $\text{Ni}_{0.75}\text{Zn}_{0.25}\text{Fe}_2\text{O}_4$ and

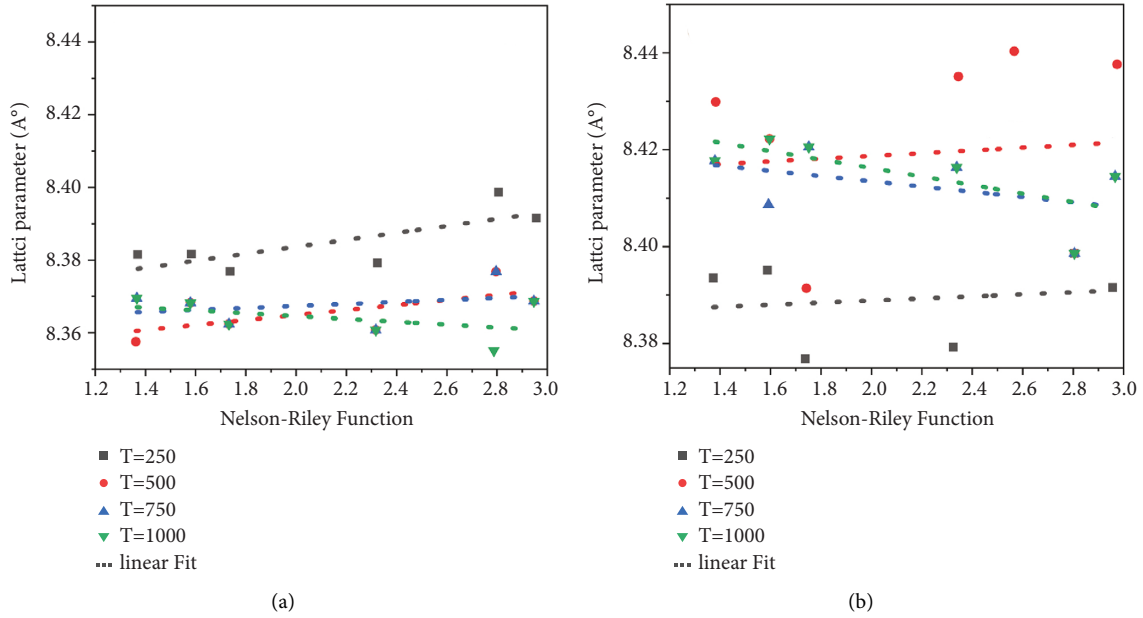


FIGURE 3: Nelson–Riley plot for $\text{Ni}_{1-x}\text{Zn}_x\text{Fe}_2\text{O}_4$ ferrites for (a) $x=0.25$ and (b) 0.75 at different annealing temperatures.

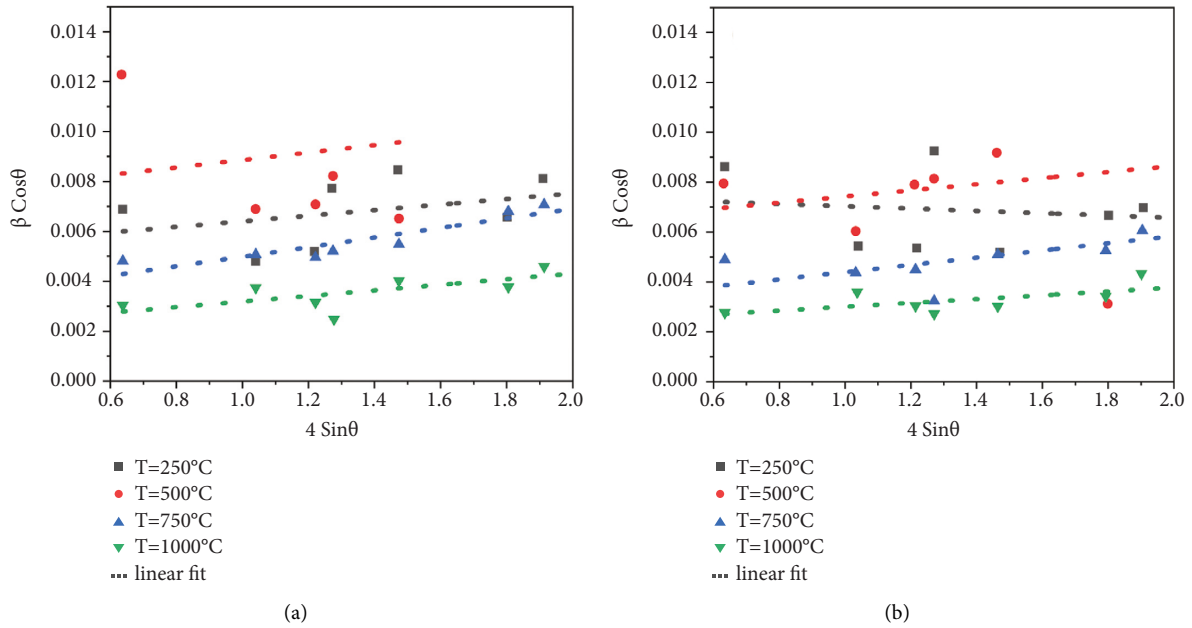


FIGURE 4: W–H plot for $\text{Ni}_{1-x}\text{Zn}_x\text{Fe}_2\text{O}_4$ ferrites at different annealing temperatures of (a) $x=0.25$ and (b) 0.75 .

$\text{Ni}_{0.25}\text{Zn}_{0.75}\text{Fe}_2\text{O}_4$, respectively. This is because of the recrystallization of nanoparticles that reduced their lattice strain broadening. The coalescence and coarsening processes cause the grain to grow, and the small grains are merged together [25]. Consequently, it clearly shows that the size of the crystallites can change by changing the annealing temperature of the sample.

From Figure 5, it is illustrated that the crystallite size (D_{Sch}) decreased with an increase in annealing temperature to 500°C , which can be referred to as an impurity phase decrease. Increasing the annealing temperature from 500°C

to 1000°C tends to increase the crystallite size from 19.58 to 43.95 nm for $\text{Ni}_{0.75}\text{Zn}_{0.25}\text{Fe}_2\text{O}_4$ and from 17.55 to 45.58 nm for $\text{Ni}_{0.25}\text{Zn}_{0.75}\text{Fe}_2\text{O}_4$.

Figure 6 illustrates that, when the Zn concentration increases, the peak positions shift towards lower angles. These results showed a larger Zn^{2+} cation and larger Fe^{2+} ions that can replace a smaller Ni^{2+} cation [31].

The lattice parameter increases when the Zn concentration is raised from 0.25 to 0.75 as shown in Table 1. This is also because the Zn^{2+} ion has a greater ionic radius than the Ni^{2+} ion. In the spinel crystal structure, tetrahedral and

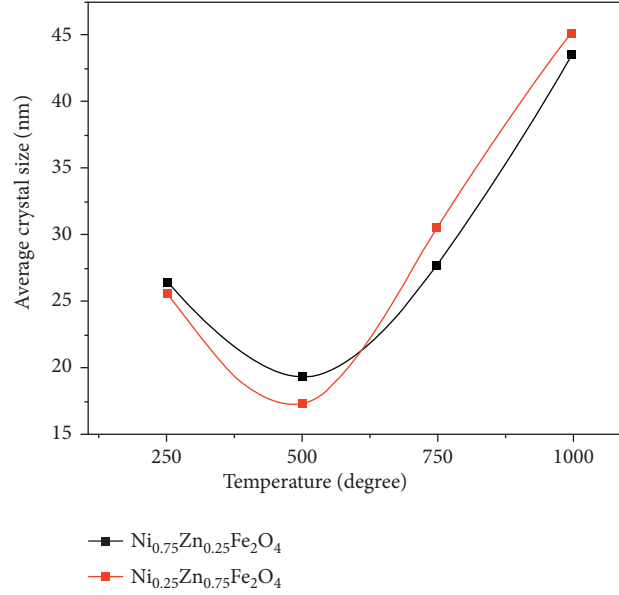


FIGURE 5: The average crystal size (D_{Sch}) of synthesized $Ni_{1-x}Zn_xFe_2O_4$ ferrites ($x=0.25$ and 0.75) with annealing temperature.

octahedral sites are preferred by larger Zn^{2+} ions and smaller Ni^{2+} ions, respectively. This evidence indicates that some Zn ions are transferred to Ni sites. Simultaneously, as Zn concentration increased, so did sample lattice volume, which makes sense given the difference in ionic radii [32–34].

For the structural examination of the samples and their cation distribution, the Rietveld refinement was used with the Fullprof software as illustrated in Figure 7. Nickel, zinc, and iron cations occupy specific Wyckoff locations 8a and 16d in cubic spinel ferrites, at $(1/8, 1/8, 1/8)$ and $(1/2, 1/2, 1/2)$, respectively [35]. The $F\bar{d}3m$ space group was used to improve the patterns of all the samples. In Figure 7, the experimental data are shown by a red open circle whereas the computed intensities are denoted by a solid black line. The bottom line shows the difference in calculated and observed intensities. A short vertical line denoted the allowable Bragg locations for the $F\bar{d}3m$ space group. Only Bragg 2θ locations are allowed for the fitting peaks in the structure.

The oxygen coordinates were treated as free parameters for refinement throughout the fitting whereas all other atomic fractional positions were treated as fixed. Other free parameters include lattice constants, isothermal parameters, occupancies, scaling factors, and form parameters. The pseudo-Voigt function was used to improve the patterns.

In order to get minimum values of reliability parameters such as profile factor (R_p), weighted residual factor (R_{wp}), and expected residual factor (R_{exp}), the XRD patterns were refined until the goodness-of-fit index (χ^2) approached unity.

Table 2 shows the Rietveld-derived cation distribution and lists the values of the determined reliability parameters and goodness-of-fit index.

Due to the random distribution of Ni, Zn, and Fe ions across tetrahedral and octahedral interstitial sites, the structure seems to be in a mixed spinel phase. Cations in the current ferrite system, such as Ni, Zn, and Fe, might have the

ability to reside in two or more valence states in their distribution.

To simplify the cation distribution, the Ni and Zn ions are considered to remain entirely in the divalent state in the cation distribution whereas the Fe ions are assumed to remain exclusively in the trivalent state in the distribution [36].

The theoretical ionic radius of a tetrahedral site (r_A) and an octahedral site (r_B) might be determined by using the following relationships based on the cations distribution [37].

$$\begin{aligned} r_A &= C_{Ni}r(Ni^{2+}) + C_{Zn}r(Zn^{2+}) + C_{Fe}r(Fe^{3+}), \\ r_B &= \frac{1}{2} [C_{Ni}r(Ni^{2+}) + C_{Zn}r(Zn^{2+}) + C_{Fe}r(Fe^{3+})]. \end{aligned} \quad (6)$$

C_{Ni} , C_{Zn} , and C_{Fe} denote the fractional concentration of Ni^{2+} , Zn^{2+} , and Fe^{3+} , respectively, at various sites taken according to cation distribution. In addition, r denotes ionic radii for appropriate ions Ni^{2+} , Zn^{2+} , and Fe^{3+} . The result is tabulated in Table 3. From Table 3, it is obvious that the r_A decreases while r_B increases as the lattice parameter grows. This variation is caused by a shift in the occupation of the (A) and (B) sites. Zinc ions (large ions) are decreased in the (A) site and increased in the (B) site for $x=0.75$ as compared to the sample of $x=0.25$.

Chemical composition, preparation environment, and heating process all influence the oxygen ion parameter (u). The computed “ u ” values for all synthesized ferrites are shown in Table 3, by using the relation [38].

$$u = \left[(r_A + r_o) \frac{1}{a\sqrt{3}} + \frac{1}{4} \right]. \quad (7)$$

The parameter “ u ” has a value of around 0.375 in the case of a perfect spinel structure. However, there were some

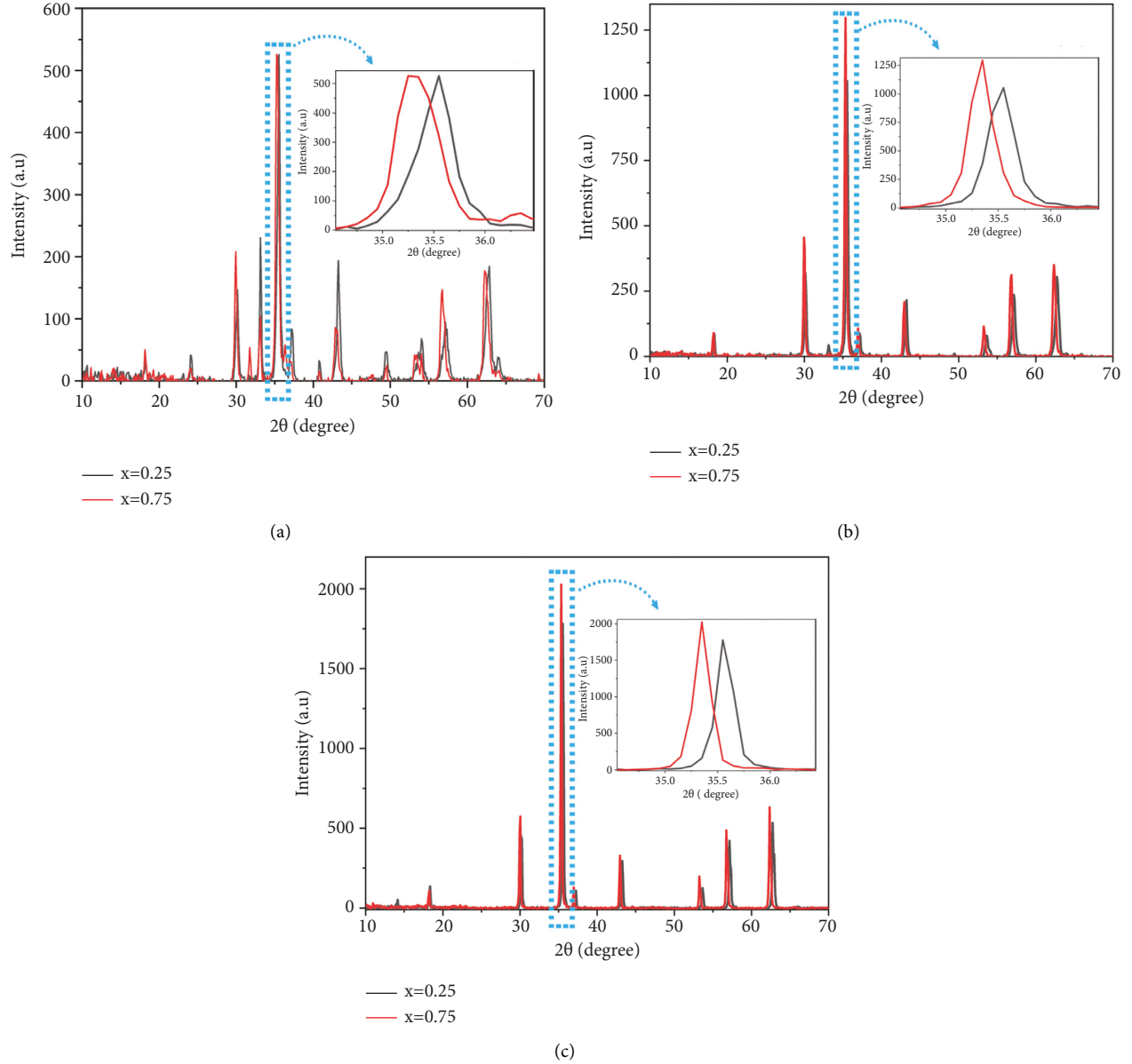


FIGURE 6: Variation of the (311) diffraction peak of $\text{Ni}_{0.75}\text{Zn}_{0.25}\text{Fe}_2\text{O}_4$ and $\text{Ni}_{0.25}\text{Zn}_{0.75}\text{Fe}_2\text{O}_4$ at the temperature of (a) 500°C , (b) 750°C , and (c) 1000°C .

variations from the ideal value for the examined samples indicating that there was deformation in the lattice.

The following equation [39] was used to compute the theoretical lattice constants for all of the samples in this study:

$$a_{th} = \frac{8}{3\sqrt{3}} [(r_A + r_o) + \sqrt{3}(r_B + r_o)]. \quad (8)$$

Table 3 contains the theoretical lattice characteristics for the samples. The theoretical lattice increased from 8.353 \AA ($x=0.25$) to 8.379 \AA ($x=0.75$). Theoretical values vary similarly to empirically determined lattice parameters.

According to the following relationships [28], the distance between magnetic ions (hopping length) at the tetrahedral site (L_A) and the octahedral site (L_B) might be calculated.

$$L_A = a \frac{\sqrt{3}}{4}, \quad (9)$$

$$L_B = a \frac{\sqrt{2}}{4}.$$

The computed L_A and L_B are shown in Table 3. The hopping lengths, L_A and L_B , rise as the concentration of Zn^{2+} ions in nickel ferrite increases. In other words, as the Zn concentration grows so does the distance between the magnetic ions. This result and the similar results of the tetrahedral and octahedral bond lengths d_{Ax} and d_{Bx} , tetrahedral edge, shared, and unshared octahedral edges (d_{AxE} , d_{BxE} , and d_{BxEU}) might be explained also by the fact that the component ions have different ionic radii [40].

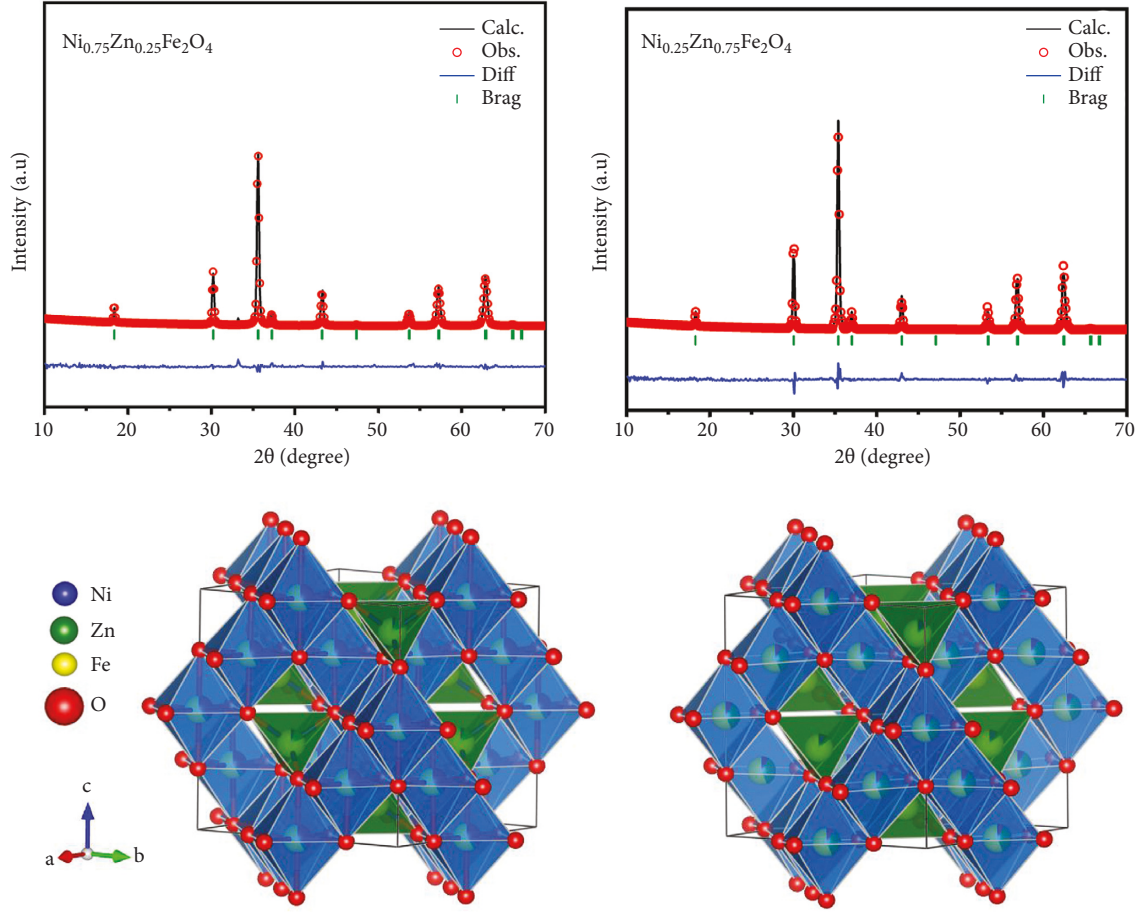


FIGURE 7: The Rietveld refinements of $\text{Ni}_{0.75}\text{Zn}_{0.25}\text{Fe}_2\text{O}_4$ and $\text{Ni}_{0.25}\text{Zn}_{0.75}\text{Fe}_2\text{O}_4$ annealed at 750°C . The diagrams in the second row show the polyhedral structure of the samples.

TABLE 2: Rietveld-derived cation distribution, profile factor (R_p), weighted residual factor (R_{wp}), expected residual factor (R_{exp}), and goodness of fit (χ^2) of $\text{Ni}_{1-x}\text{Zn}_x\text{Fe}_2\text{O}_4$ samples annealed at 750°C .

Zinc content, x	Cation distribution		R_p	R_{wp}	R_{exp}	χ^2
	A site	B site				
0.25	$(\text{Ni}_{0.052}\text{Zn}_{0.145}\text{Fe}_{0.802})$	$[\text{Ni}_{0.698}\text{Zn}_{0.105}\text{Fe}_{1.198}]$	22.90	30.00	25.49	1.39
0.75	$(\text{Ni}_{0.095}\text{Zn}_{0.052}\text{Fe}_{0.853})$	$[\text{Ni}_{0.155}\text{Zn}_{0.698}\text{Fe}_{1.147}]$	25.00	29.80	24.96	1.42

TABLE 3: Structural parameters of $\text{Ni}_{1-x}\text{Zn}_x\text{Fe}_2\text{O}_4$ ferrite ($x = 0.25$ and $x = 0.75$) annealed at 750°C , after Rietveld refinement (all in angstrom).

x	r_A	r_B	u	a_{th}	L_A	L_B	d_{Ax}	d_{Bx}	d_{AxE}	d_{BxE}	d_{BxEU}
0.25	0.503	0.665	0.3799	8.353	3.622	2.957	1.883	1.836	6.032	2.840	2.958
0.75	0.498	0.678	0.3789	8.379	3.642	2.974	1.878	1.841	6.040	2.882	2.975

$$\begin{aligned}
 d_{Ax} &= a\sqrt{3}\left(u - \frac{1}{4}\right), \\
 d_{Bx} &= a\sqrt{3u^2 - 2u + 0.375}, \\
 d_{AxE} &= a\sqrt{2}\left(2u - \frac{1}{4}\right), \\
 d_{BxE} &= a\sqrt{2}(1 - 2u), \\
 d_{BxEU} &= a\left(4u^2 - 3u + \frac{11}{16}\right)^{1/2}.
 \end{aligned} \tag{10}$$

The interionic distances and angles clearly describe the crystalline structure and have a significant influence on the magnetic interactions between ions [41]. Figure 8 depicts the cation-cation distances marked by the letters b , c , d , e , and f as well as the cation-anion distances denoted by the letters p , q , r , and s , and the corresponding bond angles are represented by θ_1 , θ_2 , θ_3 , θ_4 , and θ_5 .

The following formulas [42] are used to compute the values of all interionic distances and are tabulated in Table 4.

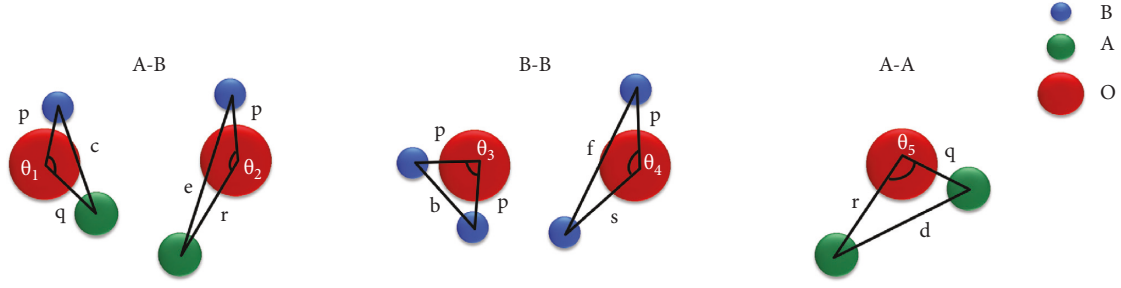


FIGURE 8: The interionic distances and interaction angles.

TABLE 4: Calculated values of interionic distances of $\text{Ni}_{1-x}\text{Zn}_x\text{Fe}_2\text{O}_4$ ferrite ($x=0.25$ and $x=0.75$) annealed at 750°C .

x	Cation-anion distances				Cation-cation distances				
	p (Å)	q (Å)	r (Å)	s (Å)	b (Å)	c (Å)	d (Å)	e (Å)	f (Å)
0.25	2.049	1.883	3.606	3.646	2.957	3.468	3.622	5.433	5.122
0.75	2.070	1.878	3.595	3.661	2.974	3.487	3.642	5.464	5.151

$$\begin{aligned}
 p &= a\left(\frac{5}{8} - u\right), \\
 q &= a\sqrt{3}\left(u - \frac{1}{4}\right), \\
 r &= a\sqrt{11}\left(u - \frac{1}{4}\right), \\
 s &= a\sqrt{3}\left(\frac{1}{3}u + \frac{1}{8}\right), \\
 b &= \left(\frac{\sqrt{2}}{4}\right)a, \\
 c &= \left(\frac{\sqrt{11}}{8}\right)a, \\
 d &= \left(\frac{\sqrt{3}}{4}\right)a, \\
 e &= \left(\frac{3\sqrt{3}}{8}\right)a, \\
 f &= \left(\frac{\sqrt{6}}{4}\right)a.
 \end{aligned} \tag{11}$$

With the exception of q and r , all interionic distances increase with Zn concentration which corresponds to an increase in unit cell volume. The cation-cation distances increase with Zn concentration at both (A) and [B] sites because of the higher atomic radii of Zn^{2+} that replace the smaller ionic radii of Ni^{2+} . Furthermore, it is seen in Table 4 that with Zn^{2+} doping, the distances between cation-cation and cation-anion increase. As a result, the $\text{Ni}_{0.25}\text{Zn}_{0.75}\text{Fe}_2\text{O}_4$ has a lower super-exchange strength than the $\text{Ni}_{0.75}\text{Zn}_{0.25}\text{Fe}_2\text{O}_4$.

By using the obtained values of the interionic distances, the bond angles θ_1 , θ_2 , θ_3 , θ_4 , and θ_5 have been determined

TABLE 5: Calculated values of bond angles of $\text{Ni}_{1-x}\text{Zn}_x\text{Fe}_2\text{O}_4$ ferrite ($x=0.25$ and $x=0.75$) annealed at 750°C .

x	θ_1 ($^\circ$)	θ_2 ($^\circ$)	θ_3 ($^\circ$)	θ_4 ($^\circ$)	θ_5 ($^\circ$)
0.25	123.67	146.43	92.35	125.81	75.38
0.75	124.02	148.10	91.81	125.68	76.36

using the expressions [42], and Table 5 shows all of these values.

$$\begin{aligned}
 \theta_1 &= \text{Cos}^{-1}\left[\frac{p^2 + q^2 - c^2}{2pq}\right], \\
 \theta_2 &= \text{Cos}^{-1}\left[\frac{p^2 + r^2 - e^2}{2pr}\right], \\
 \theta_3 &= \text{Cos}^{-1}\left[\frac{2p^2 - b^2}{2p^2}\right], \\
 \theta_4 &= \text{Cos}^{-1}\left[\frac{p^2 + s^2 - f^2}{2ps}\right], \\
 \theta_5 &= \text{Cos}^{-1}\left[\frac{r^2 + q^2 - d^2}{2rq}\right].
 \end{aligned} \tag{12}$$

Table 5 shows that, for $\text{Ni}_{0.25}\text{Zn}_{0.75}\text{Fe}_2\text{O}_4$, the values of bond angles θ_1 , θ_2 , and θ_5 rise while the values of the bond angles θ_3 and θ_4 drop. The bond angles θ_1 , θ_2 , and θ_5 are connected to A-B and A-A interactions which indicates that the strengthening of these interactions is confirmed by the increase in values of these bond angles with doping as the interaction strength is directly proportionate to the bond angle but inversely related to the bond length [41]. The super-exchange strength is increased when the A-B interaction increases. As well, a reduction in the values of θ_3 and θ_4 which is connected to B-B interactions indicates that these interactions are weakening [41].

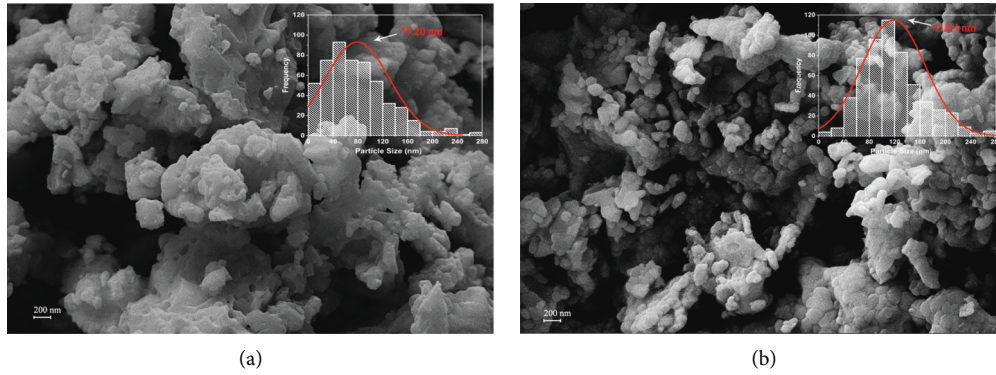


FIGURE 9: FESEM images and particle size distribution of $\text{Ni}_{1-x}\text{Zn}_x\text{Fe}_2\text{O}_4$ (a) $x = 0.25$ and (b) 0.75 annealed at 750°C .

3.2. Field Emission Scanning Electron Microscope (FESEM).

The $\text{Ni}_{0.75}\text{Zn}_{0.25}\text{Fe}_2\text{O}_4$ and $\text{Ni}_{0.25}\text{Zn}_{0.75}\text{Fe}_2\text{O}_4$ microstructures were tested by the use of FESEM as demonstrated in Figures 9(a) and 9(b), respectively. Moreover, the insets show the distribution of particle size determined from FESEM results by fitting with the normal distribution for the samples that were annealed at 750°C . It is observed from Figures 9(a) and 9(b) that the particles come in a variety of sizes and shapes. The structures of the synthesized spinel ferrite are significantly affected by the concentration of Ni^{2+} and Zn^{2+} ions which caused the distinction in the FESEM images [43]. The particles exhibit a tendency to agglomerate. The agglomeration behavior of the particles can be related to the interaction of the magnetic dipole-dipole [9, 44]. The Zn substitution in Ni ferrite has the greatest impact on the microstructure, and the grain size rises.

According to the FESEM particle size distribution from Figures 9(a) and 9(b), the estimated average ferrite nanoparticle sizes were determined to be 79.2 and 118.4 nm for $x = 0.25$ and 0.75 , respectively. Similar results were reported earlier [45]. The average size determined by XRD is less than the average size obtained from FESEM images. The diffraction signals of greater diameters are more powerful than those of smaller diameters if the nanoparticles are not fully monodispersed. This is why the size specified by XRD must always be smaller than the size specified by FESEM [7].

3.3. Energy Dispersive Spectroscopy (EDS). The elemental analysis of $\text{Ni}_{1-x}\text{Zn}_x\text{Fe}_2\text{O}_4$ nanoparticles at $x = 0.25$ and 0.75 was verified by EDS spectra, and the results are tabulated in Table 6. Figures 10(a) and 10(b) show the existence of elements utilized in the synthesizing process such as nickel, zinc, iron, and oxygen atoms. Except for these elements, there are no additional impurity components in the samples that result in defect-free and homogeneous produced samples. The ultrasonication in the manufacturing process caused the doping rate of Zn ions in Ni ferrite to become more than 180% (for $x = 0.75$) relative to earlier work [46].

3.4. Transmission Electron Microscopy (TEM).

Figures 11(a) and 11(b) illustrate the TEM micrograph for $\text{Ni}_{0.75}\text{Zn}_{0.25}\text{Fe}_2\text{O}_4$ and $\text{Ni}_{0.25}\text{Zn}_{0.75}\text{Fe}_2\text{O}_4$ nanoparticles,

TABLE 6: Elemental composition of $\text{Ni}_{1-x}\text{Zn}_x\text{Fe}_2\text{O}_4$ nanoparticles annealed at 750°C .

Elements	$x = 0.25$		$x = 0.75$			
	% Wt	%	% Wt	% Atomic		
	Expected	EDS	Atomic	Expected	EDS	
Fe	47.32	49.7	30.76	46.65	46.0	29.10
O	27.11	25.5	55.10	26.73	24.8	54.74
Ni	18.64	17.4	10.23	6.13	6.5	3.91
Zn	6.93	7.4	3.91	20.49	22.7	12.25

respectively. The majority of the particles are nearly spherical and agglomerated. The agglomeration of nanocrystals that appear in TEM images might be returned to the aggregate tendency in order to obtain a lower energy state as a result of the decrease of a particular surface area by decreasing particle interfaces [47] or may be due to the synthesis technique [43]. The results of the TEM demonstrated that the particle sizes were not uniformly distributed. Therefore, it is possible to deduce that nucleation happened in a single event which results in a nucleus size distribution [48]. The mean particle size calculated from the TEM micrograph was 58.22 nm for $x = 0.25$ and 96.16 nm for $x = 0.75$. It indicates that the grain size increases with the Zn concentration as also shown in FESEM results.

3.5. Fourier Transform Infrared Spectroscopy (FTIR).

The infrared spectroscopy (IR) spectra measured at room temperature at frequencies between 400 and 900 cm^{-1} are illustrated in Figure 12. The spectra reflected typical features of spinel ferrite with the bands attributable to stretching vibrations caused by interactions between the oxygen atom and the cations at the tetrahedral and octahedral sites [49, 50]. Two main absorption bands are commonly detected in ferrites. The higher frequency absorption band (ν_1) at around $550\sim 600\text{ cm}^{-1}$ corresponds to tetrahedral metal-oxygen (M-O) stretching vibration and the octahedral M-O stretching vibration appeared at (ν_2) band of $\sim 400\text{ cm}^{-1}$ [38, 51]. The long bond length of M-O ions at the tetrahedral and short bond length at the octahedral sites are responsible for the difference in frequency between the characteristic vibrations ν_1 and ν_2 [52].

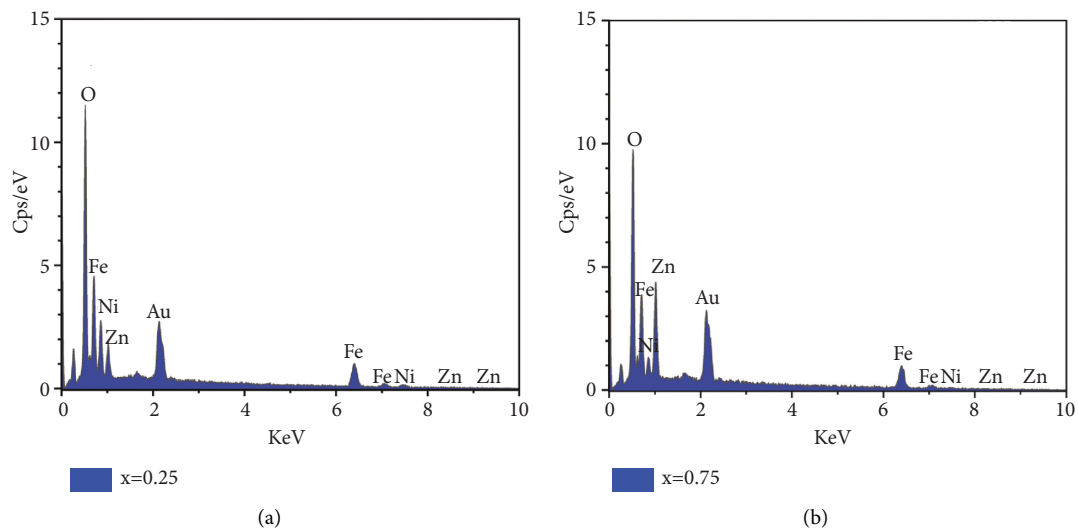


FIGURE 10: The EDS spectrum of (a) $\text{Ni}_{0.75}\text{Zn}_{0.25}\text{Fe}_2\text{O}_4$ and (b) $\text{Ni}_{0.25}\text{Zn}_{0.75}\text{Fe}_2\text{O}_4$ nanoparticles annealed at 750°C .

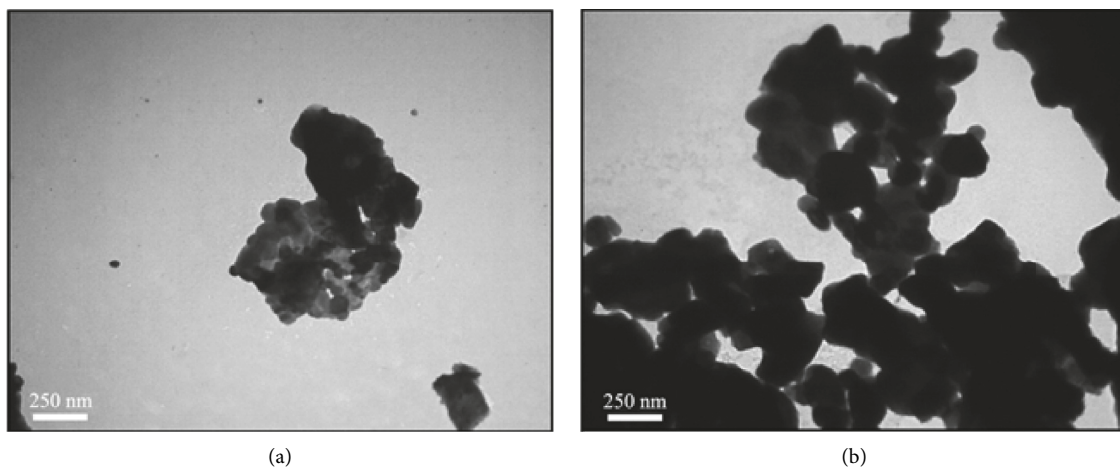


FIGURE 11: TEM images of (a) $\text{Ni}_{0.75}\text{Zn}_{0.25}\text{Fe}_2\text{O}_4$ and (b) $\text{Ni}_{0.25}\text{Zn}_{0.75}\text{Fe}_2\text{O}_4$ annealed at 750°C .

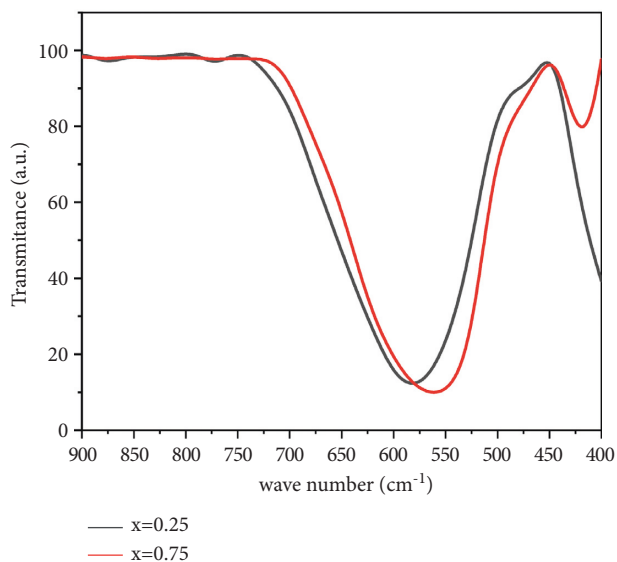


FIGURE 12: FTIR spectra of $\text{Ni}_{1-x}\text{Zn}_x\text{Fe}_2\text{O}_4$ annealed at 750°C with different Zn concentrations: $x = 0.25$ and 0.75 .

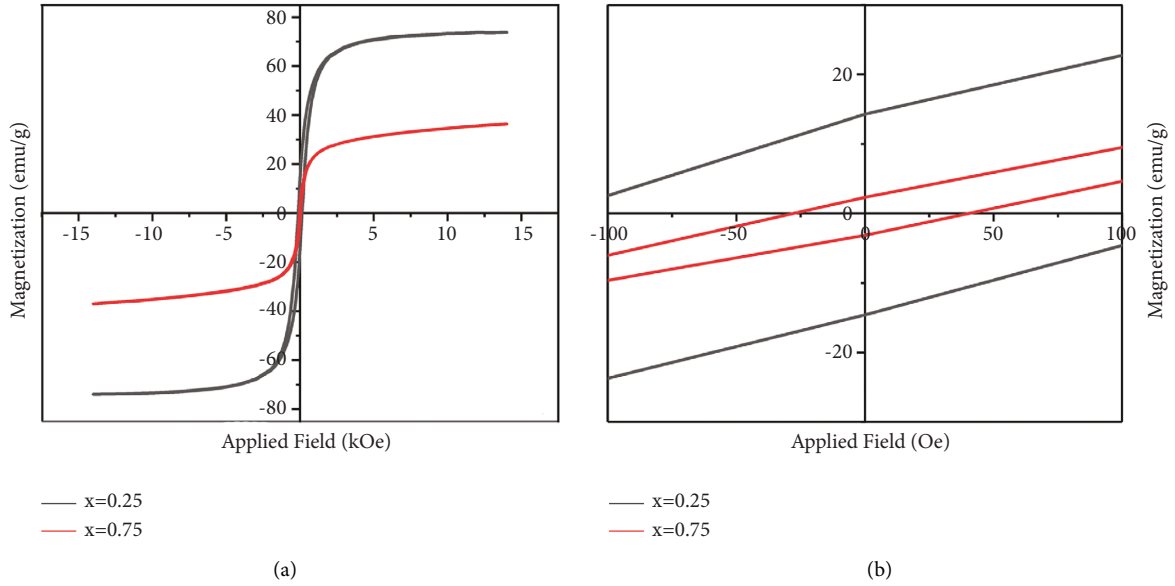


FIGURE 13: (a) $\text{Ni}_{1-x}\text{Zn}_x\text{Fe}_2\text{O}_4$ hysteresis loop at room temperature. (b) Expanded hysteresis loops.

The intensity and position of the peaks of these modes change depending on the concentration of nickel and zinc under the influence of changes in the effects of the crystalline field and strain in the lattice [53].

With increasing Zn ion concentration, band position ν_1 shifts to the lower wavenumber side, and band position ν_2 shifts towards the higher wavenumber side as shown in Figure 12. When Zn^{2+} is doped into NiFe_2O_4 , Fe^{3+} moves from the tetrahedral to the octahedral site, and it reduces the frequency of tetrahedral vibration [38]. This is because zinc has a higher atomic weight than nickel and iron. The effective atomic weight at tetrahedral sites increases as Zn concentrations rise. According to the inverse relationship between frequency and the group weights, this group's related band shifts toward a lower frequency range.

3.6. Vibrating Sample Magnetometer (VSM). A VSM was used to estimate the magnetic characteristics of the samples by applying a magnetic field of 14 kOe which indicates that the samples exhibited magnetic behavior. Magnetizations (M) against magnetic field (H) plots (hysteresis loop) of prepared Ni-Zn samples are demonstrated in Figure 13. The magnitudes of the saturation magnetization (M_s), remanent magnetization (M_r), loop squareness ratio (M_r/M_s), coercivity (H_c), and magnetic moment (n_B) were determined from hysteresis loops and tabulated in Table 7.

Figure 13 demonstrates the magnetic behavior of the $\text{Ni}_{0.75}\text{Zn}_{0.25}\text{Fe}_2\text{O}_4$ and $\text{Ni}_{0.25}\text{Zn}_{0.75}\text{Fe}_2\text{O}_4$ ferrite nanoparticles. The ferrimagnetic behavior of soft magnetic material was observed in the samples [54]; that is, nonpermanent magnetic materials which are due to their small M_r and H_c values are very easily magnetized and demagnetized at low field values. This shows the narrow magnetic hysteresis loop that has been completely formed. Cationic magnetic moments are

produced at tetrahedral and octahedral sites by the superexchange interaction between metal cations which are responsible for the magnetic properties [55]. There are several factors that the magnetic behavior of spinel ferrites depends on such as synthesis method, grain size, chemical composition, and the cation distribution [56, 57].

It was seen that all the magnetic parameters were decreased with the decrease of Zn concentration in the Ni ferrite matrix as shown in Table 7. This decrease in magnetic parameters was caused primarily by the substitution of magnetic Ni ions with nonmagnetic Zn ions [44].

Magnetization is caused by the formation of magnetic moments. The distribution of magnetic ions in the spinel structure determines the net magnetic moment. The magnetic moment in a Bhor magneton is calculated by the following relation [58], and the results are presented in Table 7.

$$n_B = \frac{M_w M_s}{5585}. \quad (13)$$

The cation distribution between (A) and [B] sites affects magnetism. At 0 K, when both sides' spins are antiferromagnetically coupled, each formula unit has a net magnetic moment. Following Néel's ferrimagnetism model, the magnetic moments of ions on (A) and [B] sites are oriented antiparallel to one another, and their spins are collinear. The theoretical magnetic moment per formula unit $n_B(x)$ is defined as follows [59]:

$$n_B(x) = M_B(x) - M_A(x), \quad (14)$$

where $M_B(x)$ and $M_A(x)$ are the sublattice magnetic moments for the [B] and (A) sites, respectively.

Theoretical magnetic moment values were computed as a function of Zn concentration by using the ionic magnetic moments and the cation distribution. The findings are stated in Table 7.

TABLE 7: The saturation magnetization (M_s), remanent magnetization (M_r), loop squareness (M_r/M_s), coercivity (H_c), and observed and calculated magneton number (n_B) of $Ni_{1-x}Zn_xFe_2O_4$ nanoparticles annealed at 750°C.

Zn content, x	Cation distribution	M_s (emu/g)	M_r (emu/g)	M_r/M_s	H_c (Oe)	n_B (μ_B)	
						Obs. (VSM)	Cal. (XRD)
0.25	($Ni_{0.052}Zn_{0.145}Fe_{0.802}$) ($Ni_{0.698}Zn_{0.105}Fe_{1.198}$)	73.7	14.3	0.19	138.2	3.12	3.27
0.75	($Ni_{0.095}Zn_{0.052}Fe_{0.853}$) ($Ni_{0.155}Zn_{0.698}Fe_{1.147}$)	36.4	2.3	0.06	40.5	1.56	1.59

The saturation magnetization of $Ni_{0.75}Zn_{0.25}Fe_2O_4$ and $Ni_{0.25}Zn_{0.75}Fe_2O_4$ are 73.7 and 36.4 emu/g, respectively. The high M_s of $Ni_{0.75}Zn_{0.25}Fe_2O_4$ is because of the substitution of Zn into $NiFe_2O_4$. Fe^{3+} ions of (A) site migrate to [B] sites, resulting in the change in the magnetic moment, decreasing at site (A), and increasing at site [B], therefore raising the overall magnetization [60]. The magnetic saturation is low in $Ni_{0.25}Zn_{0.75}Fe_2O_4$ due to the nonmagnetic nature of Zn^{2+} . Due to the negative B-B cross-interaction, the moments of the site [B] are unable to align antiparallel to themselves [61]. This behavior might possibly be explained by the presence of a high number of Zn^{2+} ions in the tetrahedral sites which weakens the magnetic moment of this site, increases the spin canting effect, and results in a significant decrease in the total magnetization [43]. The coercivity, retentivity, and magnetic moment of the samples change in a similar way to saturation magnetization. Small values of the loop squareness ratio (below 0.5) refer to the existence of single-domain particles in the samples [62].

4. Conclusions

The sol-gel auto-combustion was utilized to manufacture a cubic spinel structure of $Ni_{1-x}Zn_xFe_2O_4$ nanoparticles with $x = 0.25$ and 0.75. The crystal size increased as the annealing temperature was raised. Zn doping increased the lattice parameter because Zn^{2+} has larger ionic radii than Ni^{2+} . According to the cation distribution study, it was found that the substituted Zn^{2+} was distributed throughout the A and B sites resulting in the mixed spinel structure. The FESEM and TEM images showed that as the Zn concentration rises, the grain size grows larger. The purity of the produced Ni-Zn nanoferrites and a high rate, more than 180%, of doped zinc ions were verified by an EDS analysis. In FTIR spectra, the presence of two strong absorption bands around 550~600 cm^{-1} (ν_1) and ~400 cm^{-1} (ν_2) revealed the formation of ferrite samples, and ν_1 shifted to a lower frequency whereas ν_2 shifted to a higher frequency with increasing Zn content. The $Ni_{0.75}Zn_{0.25}Fe_2O_4$ sample exhibited the highest values of M_s , M_r , H_c , and n_B due to cation distribution.

Data Availability

The manuscript includes all data, and we don't have any data as part of the supplementary information.

Conflicts of Interest

The authors declare that they have no known competing financial interests or personal relationships that could have appeared to influence the work reported in this paper.

Acknowledgments

The authors are grateful to the Nanotechnology Research Laboratory, Department of Physics, University of Sulaimani, for laboratory support.

References

- [1] M. Junaid, M. A. Khan, S. A. Abubshait et al., "Structural, spectral, dielectric and magnetic properties of indium substituted copper spinel ferrites synthesized via sol gel technique," *Ceramics International*, vol. 46, no. 17, pp. 27410–27418, 2020.
- [2] P. P. Mohapatra, S. Pittala, and P. Dobbidi, "Temperature dependent broadband dielectric, magnetic and electrical studies on Li1-Mg₂Fe₅-O₈ for microwave devices," *Journal of Materials Research and Technology*, vol. 9, no. 3, pp. 2992–3004, 2020.
- [3] R. Jose, R. Jothi, and N. S. N. Jothi, "The synthesis and characterisation of curcumin loaded Ag (1-X) Ni X Fe₂O₄ for drug delivery," *Materials Technology*, vol. 36, no. 6, pp. 339–346, 2021.
- [4] R. R. Powar, V. D. Phadtare, V. G. Parale et al., "Effect of zinc substitution on magnesium ferrite nanoparticles: structural, electrical, magnetic, and gas-sensing properties," *Materials Science and Engineering: B*, vol. 262, Article ID 114776, 2020.
- [5] P. S. Mkwae, I. Kortidis, R. E. Kroon et al., "Insightful acetone gas sensing behaviour of Ce substituted MgFe₂O₄ spinel nano-ferrites," *Journal of Materials Research and Technology*, vol. 9, no. 6, pp. 16252–16269, 2020.
- [6] K. K. Kefeni, T. A. M Msagati, and B. B. Mamba, "Ferrite nanoparticles: synthesis, characterisation and applications in electronic device," *Materials Science and Engineering: B*, vol. 215, pp. 37–55, 2017.
- [7] Y. Mouhib, M. Belaiche, and S. Briche, "Elaboration, characterization, and magnetic properties of Ni_{0.5}Zn_{0.5}Fe₂O₄ nanoparticles of high purity using molten salts technique," *Physica Status Solidi (a)*, vol. 215, no. 23, Article ID 1800469, 2018.
- [8] S. Song, Q. Song, J. Li, V. R. Mudinepalli, and Z. Zhang, "Characterization of submicrometer-sized NiZn ferrite prepared by spark plasma sintering," *Ceramics International*, vol. 40, no. 5, pp. 6473–6479, 2014.
- [9] A. Bajorek, C. Berger, M. Dulski et al., "Microstructural and magnetic characterization of Ni_{0.5}Zn_{0.5}Fe₂O₄ ferrite nanoparticles," *Journal of Physics and Chemistry of Solids*, vol. 129, pp. 1–21, 2019.
- [10] K. Momma and F. Izumi, "VESTA: a three-dimensional visualization system for electronic and structural analysis," *Journal of Applied Crystallography*, vol. 41, no. 3, pp. 653–658, 2008.
- [11] I. Starko, T. Tatarchuk, and M. Bououdina, "La-doped Ni_{0.5}Co_{0.5}Fe₂O₄ nanoparticles: effect of cobalt precursors on structure and morphology," *Molecular Crystals and Liquid Crystals*, vol. 674, no. 1, 2018.

- [12] T. Tatarchuk, A. Shyichuk, Z. Sojka et al., "Green synthesis, structure, cations distribution and bonding characteristics of superparamagnetic cobalt-zinc ferrites nanoparticles for Pb (II) adsorption and magnetic hyperthermia applications," *Journal of Molecular Liquids*, vol. 328, Article ID 115375, 2021.
- [13] M. Atif, "Synthesis and temperature dependent magnetic properties of nanocrystalline $\text{Ni}_{0.5}\text{Zn}_{0.5}\text{Fe}_2\text{O}_4$ ferrites," *Materials Research Express*, vol. 6, no. 7, Article ID 076104, 2019.
- [14] M. Kachniarz and J. Salach, "Characterization of magnetoelastic properties of Ni-Zn ferrite in wide range of magnetizing fields for stress sensing applications," *Measurement*, vol. 168, Article ID 108301, 2021.
- [15] R. M. Freire, P. G. C. Freitas, W. S. Galvao et al., "Nanocrystal growth, magnetic and electrochemical properties of NiZn ferrite," *Journal of Alloys and Compounds*, vol. 738, pp. 206–217, 2018.
- [16] J. F. Odah, "Studying the structure, the electric and magnetic properties of Ni-Zn ferrites," *International Journal of Advanced Research*, vol. 4, pp. 560–569, 2016.
- [17] N. Aggarwal and S. B. Narang, "Magnetic characterization of Nickel-Zinc spinel ferrites along with their microwave characterization in Ku band," *Journal of Magnetism and Magnetic Materials*, vol. 513, Article ID 167052, 2020.
- [18] A. A. El-Fadl, A. M. Hassan, M. H. Mahmoud et al., "Synthesis and magnetic properties of spinel $\text{Zn}_{1-x}\text{Ni}_x\text{Fe}_2\text{O}_4$ ($0.0 \leq x \leq 1.0$) nanoparticles synthesized by microwave combustion method," *Journal of Magnetism and Magnetic Materials*, vol. 471, pp. 192–199, 2019.
- [19] C. A. P. Gómez, C. A. B. Meneses, and J. A. Jaén, "Raman, infrared and Mössbauer spectroscopic studies of solid-state synthesized Ni-Zn ferrites," *Journal of Magnetism and Magnetic Materials*, vol. 505, Article ID 166710, 2020.
- [20] M. Derakhshani, E. Taheri-Nassaj, M. Jazirehpour, and S. M. Masoudpanah, "Enhanced electromagnetic wave absorption performance of Ni-Zn ferrite through the added structural macroporosity," *Journal of Materials Research and Technology*, vol. 16, pp. 700–714, 2022.
- [21] S. Zahi, A. R. Daud, and M. Hashim, "A comparative study of nickel-zinc ferrites by sol-gel route and solid-state reaction," *Materials Chemistry and Physics*, vol. 106, no. 3, pp. 452–456, 2007.
- [22] R. B. Assis, M. R. D. Bomio, R. M. Nascimento, C. A. Paskocimas, E. Longo, and F. V. Motta, "Rapid calcination of ferrite $\text{Ni}_{0.75}\text{Zn}_{0.25}\text{Fe}_2\text{O}_4$ by microwave energy," *Journal of Thermal Analysis and Calorimetry*, vol. 118, no. 1, pp. 277–285, 2014.
- [23] Z. Saeed and B. Azhdar, "A novel method for synthesizing narrow particle size distribution of holmium-doped strontium hexaferrite by sol-gel auto-combustion," *Materials Research Express*, vol. 7, no. 4, Article ID 045006, 2020.
- [24] S. M. Olhero, D. Soma, V. S. Amaral, T. W. Button, F. J. Alves, and J. M. F. Ferreira, "Co-precipitation of a Ni-Zn ferrite precursor powder: effects of heat treatment conditions and deagglomeration on the structure and magnetic properties," *Journal of the European Ceramic Society*, vol. 32, no. 10, pp. 2469–2476, 2012.
- [25] E. Suharyadi, S. H. Pratiwi, I. P. T. Indrayana, T. Kato, S. Iwata, and K. Ohto, "Effects of annealing temperature on microstructural, magnetic properties, and specific absorption rate of Zn-Ni ferrite nanoparticles," *Materials Research Express*, vol. 8, no. 3, Article ID 036101, 2021.
- [26] U. Holzwarth and N. Gibson, "The Scherrer equation versus the 'Debye-Scherrer equation'," *Nature Nanotechnology*, vol. 6, no. 9, p. 534, 2011.
- [27] M. Ajmal, M. U. Islam, G. A. Ashraf, M. A. Nazir, and M. I. Ghouri, "The influence of Ga doping on structural magnetic and dielectric properties of $\text{NiCr}_{0.2}\text{Fe}_{1.8}\text{O}_4$ spinel ferrite," *Physica B: Condensed Matter*, vol. 526, pp. 149–154, 2017.
- [28] R. N. Chikhale, S. A. Kanade, and P. G. Bhatia, "Low temperature rapid sol-gel auto-combustion synthesis and structural, morphological and magnetic study of nickel substituted cobalt nano ferrites," *Phase Transitions*, vol. 94, pp. 1–16, 2021.
- [29] D. Venkatesh, M. S. R. Prasad, B. Rajesh Babu, K. V. Ramesh, and K. Trinath, "Effect of sintering temperature on the micro strain and magnetic properties of Ni-Zn nanoferrites," *Journal of Magnetism*, vol. 20, no. 3, pp. 229–240, 2015.
- [30] M. Zhang, Z. Zi, Q. Liu et al., "Size effects on magnetic properties of prepared by sol-gel method," *Advances In Materials Science And Engineering*, vol. 2013, Article ID 609819, , 2013.
- [31] U. Wongpratad, S. Meansiri, and E. Swatsitang, "Local structure and magnetic property of $\text{Ni}_{1-x}\text{Zn}_x\text{Fe}_2\text{O}_4$ ($x = 0, 0.25, 0.50, 0.75, 1.00$) nanoparticles prepared by hydrothermal method," *Microelectronic Engineering*, vol. 126, pp. 19–26, 2014.
- [32] J. Hwang, M. Choi, H.-S. Shin, B.-K. Ju, and M. Chun, "Structural and magnetic properties of NiZn ferrite nanoparticles synthesized by a thermal decomposition method," *Applied Sciences*, vol. 10, no. 18, 2020.
- [33] N.-N. Jiang, Y. Yang, Y.-X. Zhang, J.-P. Zhou, P. Liu, and C.-Y. Deng, "Influence of zinc concentration on structure, complex permittivity and permeability of Ni-Zn ferrites at high frequency," *Journal of Magnetism and Magnetic Materials*, vol. 401, pp. 370–377, 2016.
- [34] S. B. Khan, S. Irfan, and S.-L. Lee, "Influence of Zn²⁺ doping on Ni-based nanoferrites; ($\text{Ni}_{1-x}\text{Zn}_x\text{Fe}_2\text{O}_4$)," *Nanomaterials*, vol. 9, no. 7, p. 1024, 2019.
- [35] B. Nandan, M. C. Bhatnagar, and S. C. Kashyap, "Cation distribution in nanocrystalline cobalt substituted nickel ferrites: X-ray diffraction and Raman spectroscopic investigations," *Journal of Physics and Chemistry of Solids*, vol. 129, pp. 298–306, 2019.
- [36] B. P. Rao, B. Dhanalakshmi, S. Ramesh, and P. S. V. Subba Rao, "Cation distribution of Ni-Zn-Mn ferrite nanoparticles," *Journal of Magnetism and Magnetic Materials*, vol. 456, pp. 444–450, 2018.
- [37] C. A. P. Gómez, C. A. B. Meneses, and A. Matute, "Structural parameters and cation distributions in solid state synthesized Ni-Zn ferrites," *Materials Science and Engineering: B*, vol. 236, pp. 48–55, 2018.
- [38] R. Sharma and S. Singhal, "Structural, magnetic and electrical properties of zinc doped nickel ferrite and their application in photo catalytic degradation of methylene blue," *Physica B: Condensed Matter*, vol. 414, pp. 83–90, 2013.
- [39] M. B. Mohamed and M. Yehia, "Cation distribution and magnetic properties of nanocrystalline gallium substituted cobalt ferrite," *Journal of Alloys and Compounds*, vol. 615, pp. 181–187, 2014.
- [40] D. S. Nikam, S. V. Jadhav, V. M. Khot et al., "Cation distribution, structural, morphological and magnetic properties of $\text{Co}_{1-x}\text{Zn}_x\text{Fe}_2\text{O}_4$ ($x = 0-1$) nanoparticles," *RSC Advances*, vol. 5, no. 3, pp. 2338–2345, 2015.

- [41] S. Debnath, A. Das, and R. Das, "Effect of cobalt doping on structural parameters, cation distribution and magnetic properties of nickel ferrite nanocrystals," *Ceramics International*, vol. 47, no. 12, pp. 16467–16482, 2021.
- [42] I. B. Elius, S. Hossain, M. S. Aktar et al., "Structural and magnetic characterizations of $\text{Ni}_x\text{Cu}_{0.8-x}\text{Zn}_{0.2}\text{Fe}_2\text{O}_4$ spinel ferrites," *Ferroelectrics*, vol. 572, no. 1, pp. 36–50, 2021.
- [43] A. B. Mapossa, J. Dantas, M. R. Silva, R. H. G. A. Kiminami, A. C. F. M. Costa, and M. O. Daramola, "Catalytic performance of NiFe_2O_4 and $\text{Ni}_{0.3}\text{Zn}_{0.7}\text{Fe}_2\text{O}_4$ magnetic nanoparticles during biodiesel production," *Arabian Journal of Chemistry*, vol. 13, no. 2, pp. 4462–4476, 2020.
- [44] S. A. Jadhav, S. B. Somvanshi, M. V. Khedkar, S. R. Patade, and K. M. Jadhav, "Magneto-structural and photocatalytic behavior of mixed Ni-Zn nano-spinel ferrites: visible light-enabled active photodegradation of rhodamine B," *Journal of Materials Science: Materials in Electronics*, vol. 31, no. 14, pp. 11352–11365, 2020.
- [45] I. I. Shamray, V. Yu Buz'ko, and A. I. Goryachko, "Changes in the structure and properties of nickel-zinc spinel nanoferrites series for 3D-printing," *IOP Conference Series: Materials Science and Engineering*, vol. 969, no. 1, Article ID 012101, 2020.
- [46] C. O. Ehi-Eromosele, B. I. Ita, E. E. Iweala, S. A. Adalikwu, and P. A. L. Anawe, "Magneto-structural properties of Ni-Zn nanoferrites synthesized by the low-temperature auto-combustion method," *Bulletin of Materials Science*, vol. 38, no. 5, pp. 1465–1472, 2015.
- [47] S. Thankachan, B. P. Jacob, S. Xavier, and E. M. Mohammed, "Effect of samarium substitution on structural and magnetic properties of magnesium ferrite nanoparticles," *Journal of Magnetism and Magnetic Materials*, vol. 348, pp. 140–145, 2013.
- [48] A. C. F. M. Costa, E. Tortella, M. R. Morelli, and R. H. G. A. Kiminami, "Synthesis, microstructure and magnetic properties of Ni-Zn ferrites," *Journal of Magnetism and Magnetic Materials*, vol. 256, no. 3, pp. 174–182, 2003.
- [49] M. Atif and M. Nadeem, "Sol-gel synthesis of nanocrystalline $\text{Zn}_{1-x}\text{Ni}_x\text{Fe}_2\text{O}_4$ ceramics and its structural, magnetic and dielectric properties," *Journal of Sol-Gel Science and Technology*, vol. 72, pp. 615–626, 2014.
- [50] M. Rahimi, P. Kameli, M. Ranjbar, H. Hajihashemi, and H. Salamati, "The effect of zinc doping on the structural and magnetic properties of $\text{Ni}_{1-x}\text{Zn}_x\text{Fe}_2\text{O}_4$," *Journal of Materials Science*, vol. 48, pp. 2969–2976, 2013.
- [51] X. He, G. Song, and J. Zhu, "Non-stoichiometric NiZn ferrite by sol-gel processing," *Materials Letters*, vol. 59, no. 15, pp. 1941–1944, 2005.
- [52] P. S. Hedao, D. S. Badwaik, and K. G. Rewatkar, "Morphological study and optoelectrical properties of Zn^{2+} substituted nickel ferrite nanoparticles," *Materials Today Proceedings*, vol. 29, pp. 1033–1038, 2020.
- [53] G. S. Shahane, A. Kumar, M. Arora, R. P. Pant, and K. Lal, "Synthesis and characterization of Ni-Zn ferrite nanoparticles," *Journal of Magnetism and Magnetic Materials*, vol. 322, no. 8, pp. 1015–1019, 2010.
- [54] M. M. Ismail and N. A. Jaber, "Influences of cation distribution of zinc substituted on inverse spinel nickel ferrite nanoparticle for superparamagnetic approach," *Surface Review and Letters*, vol. 25, Article ID 1850076, 2018.
- [55] De-P. Yang, L. K. Lavoie, Y. Zhang, Z. Zhang, and S. Ge, "Mössbauer spectroscopic and X-ray diffraction studies of structural and magnetic properties of heat-treated ($\text{Ni}_{0.5}\text{Zn}_{0.5}$) Fe_2O_4 nanoparticles," *Journal of Applied Physics*, vol. 93, no. 10, pp. 7492–7494, 2003.
- [56] P. S. Hedao, D. S. Badwaik, S. M. Suryawanshi, and K. G. Rewatkar, "Structural and magnetic studies of Zn doped nickel nanoferrites synthesized by sol-gel auto combustion method," *Materials Today Proceedings*, vol. 15, pp. 416–423, 2019.
- [57] B. Rabi, A. Essoumhi, M. Sajieddine et al., "Structural, magnetic and magnetocaloric study of $\text{Ni}_{0.5}\text{Zn}_{0.5}\text{Fe}_2\text{O}_4$ spinel," *Applied Physics A*, vol. 126, pp. 1–11, 2020.
- [58] R. Sankaranarayanan, S. Shailajha, M. S. K. Mubina, and C. P. Anilkumar, "Effect of Zn^{2+} ions on structural, optical, magnetic, and impedance response of $\text{Zn}_x\text{Ni}_{1-x}\text{Fe}_2\text{O}_4$ core materials prepared by two-step polyacrylamide gel method," *Journal of Materials Science: Materials in Electronics*, vol. 31, pp. 11833–11846, 2020.
- [59] H. Kavas, A. Baykal, M. S. Toprak, Y. Köseoğlu, M. Sertkol, and B. Aktaş, "Cation distribution and magnetic properties of Zn doped NiFe_2O_4 nanoparticles synthesized by PEG-assisted hydrothermal route," *Journal of Alloys and Compounds*, vol. 479, no. 2, pp. 49–55, 2009.
- [60] B. H. Guan, M. H. Zahari, and L. K. Chuan, "Structural and magnetic properties of $\text{Ni}_{1-x}\text{Zn}_x\text{Fe}_2\text{O}_4$ synthesized through the sol-gel method," *AIP Conference Proceedings*, vol. 1787, 2016.
- [61] M. A. Ahmed, N. Okasha, and M. Gabal, "Transport and magnetic properties of Co-Zn-La ferrite," *Materials Chemistry and Physics*, vol. 83, no. 1, pp. 107–113, 2004.
- [62] A. Sadaqat, M. Almessiere, Y. Slimani et al., "Structural, optical and magnetic properties of Tb^{3+} substituted Co nanoferrites prepared via sonochemical approach," *Ceramics International*, vol. 45, no. 17, pp. 22538–22546, 2019.